

Article

Not peer-reviewed version

---

# Lidar Optical and Microphysical Characterization of Tropospheric and Stratospheric Fire Smoke Layers Due to Canadian Wildfires Passing over Naples (Italy)

---

[Riccardo Damiano](#) , [Salvatore Amoruso](#) , [Alessia Sannino](#) , [Antonella Boselli](#) \*

Posted Date: 21 December 2023

doi: 10.20944/preprints202312.1681.v1

Keywords: Remote Sensing, Canadian Fire, Microphysical Properties



Preprints.org is a free multidiscipline platform providing preprint service that is dedicated to making early versions of research outputs permanently available and citable. Preprints posted at Preprints.org appear in Web of Science, Crossref, Google Scholar, Scilit, Europe PMC.

Copyright: This is an open access article distributed under the Creative Commons Attribution License which permits unrestricted use, distribution, and reproduction in any medium, provided the original work is properly cited.

Article

# Lidar Optical and Microphysical Characterization of Tropospheric and Stratospheric Fire Smoke Layers Due to Canadian Wildfires Passing over Naples (Italy)

Riccardo Damiano <sup>1</sup>, Salvatore Amoruso <sup>1</sup>, Alessia Sannino <sup>1</sup>, Antonella Boselli <sup>2</sup> and \*

<sup>1</sup> Dipartimento di Fisica "Ettore Pancini", Complesso Universitario di Monte S. Angelo, Via Cintia, I-80126 Napoli (Italy).

<sup>2</sup> Consiglio Nazionale delle Ricerche Istituto di Metodologie per l'Analisi Ambientale, C.da S. Loja, 85050 Tito Scalo, Potenza (Italy).

\* Correspondence: Dr. Antonella Boselli, antonella.boselli@cnr.it

**Abstract:** In Summer 2017, huge wildfires in the British Columbia region (Canada) led to the injection of a remarkably high concentration of biomass burning aerosol in the atmosphere. These aerosol masses reached the city of Naples, Italy, since the end of August 2017, where they were characterized by means of a multiwavelength lidar and a sun-sky-lunar photometer. Here we report on the optical and microphysical properties of this aerosol in an intriguing condition, occurring on 4<sup>th</sup> September 2017, which is characterized by an interesting multi-layered vertical distribution of the aerosol. The Lidar profiles highlighted the presence of four aerosol layers, with two located in the lower troposphere and other two at stratospheric altitudes. A rather thorough characterization of the biomass burning aerosol was carried out. The aerosol depolarization ratio showed an increasing dependence on the altitude with averaged values of 2-4% for the tropospheric layers, which are indicative of almost spherical smoke particles, and larger values in the stratospheric layers, suggestive of aspheric particles. Lidar-derived size distributions were retrieved for the first three aerosol layers, highlighting a higher particle concentration in the fine mode fraction for the layers observed at higher altitude. A dominance of fine particles in the atmosphere (Fine Mode Fraction > 0.8) with low absorption properties (absorption AOD < 0.0025 and SSA > 0.97) was also observed over the whole atmospheric column by sun-photometer data. The space-resolved results provided by the lidar data are consistent with the columnar features retrieved by the AERONET sun-photometer, thus evidencing the reliability and capability of lidar characterization of atmospheric aerosol in a very interesting condition of multiple aerosol layers originating from Canadian fires overpassing the observation station.

**Keywords:** remote sensing; canadian fire; microphysical properties

## 1. Introduction

Biomass burning aerosol mainly originates from wildfires and constitutes an important natural source of the atmospheric aerosol that influences the Earth's radiation budget and affects atmospheric circulation and regional climate [1,2]. It is primarily composed by light-absorbing components, as brown and black carbon, representing the main source of organic aerosol in the atmosphere [3]. Biomass burning aerosol plays an important role in radiation budget, because it influences the scattering or absorption of the solar radiation and acts as cloud condensation nuclei or ice nuclei. Moreover, its radiative effect can be either direct or indirect [4]. The chemical and physical properties of biomass burning aerosol can vary during the transport in the atmosphere, as a consequence of both ageing effects and mixing with aerosol originated by other sources, and significantly influence the impact of wildfires on climate changes and air quality [5]. The vertical transport of smoke particles through the tropopause remains hitherto unclear, and hence still under investigation; recent studies have reported observation or modeling analyses of smoke particles layers produced by late wildfire episodes in the lower stratosphere [6–10]. In this altitude range, the particles are confined for a long

time and can reach areas located many kilometers far away from their source region. During the transport, the particles influence the atmospheric circulation and interact with clouds, eventually reducing the precipitation rate [11]. Moreover, major fire events can even lead to stratospheric ozone depletion in Arctic and Antarctic regions [12].

Lidars have been extensively used to study long range smoke transport, being able to retrieve the vertical profile of their optical and microphysical properties. Lidar measurements are usually analyzed in synergy with data provided by other instruments, like sun photometers [13–15], spaceborne instruments [7,16] or nephelometers [17].

In the Summer of 2017, huge wildfires in the British Columbia region (Canada) led to the injection of an unusually high concentration of biomass burning aerosol in the atmosphere, which was observed even over Europe in the following weeks. An uncommon load of smoke was released on 12<sup>th</sup> August 2017 in the troposphere and lower stratosphere over the western area, and during the successive weeks it was transported by air flow all over the northern hemisphere, reaching also the tropics [18]. Its presence was detected by many European observation stations during the following weeks. In Leipzig on 22<sup>nd</sup> August 2017, three lidars analyzed the optical and microphysical properties of two atmospheric smoke layers: one in the troposphere and one in the lower stratosphere; the former showed smaller and less depolarizing particles than the latter one [19]. In Kosetice, Czech Republic, a smoke layer raising from 12 km to 16 km altitude was detected by a lidar from 20<sup>th</sup> to 23<sup>rd</sup> August 2017 [6]. Ref. [7] reported on the observation of a smoke layer from the spaceborne CALIOP lidar and the ground-based lidars located at the Observatoire de Haute-Provence, in southern France, whereas Ref. [9] characterized the smoke plume with simultaneous lidar and sun-photometer observations in Lille and Palaiseau. Smoke layers were observed up to 20 km altitude and persisted in the atmosphere until the first months of 2018 [18,20].

Between 29<sup>th</sup> December 2019 and 4<sup>th</sup> January 2020, another noteworthy outbreak of pyrocumulonimbus, due to the Australian bushfire season, was observed in the Southern Hemisphere; it was dubbed as the Black summer due to the unprecedented intensity of the wildfires, which caused vast land damages [21]. The smoke particles arrived up to the lower stratosphere and the transportation event was observed by lidars located in Punta Arenas (Chile) and Río Grande (Argentina) [22,23].

Here we report on aged biomass burning aerosol, coming from North America during the Summer of 2017, observed over the observation station of Naples, Italy. The aerosol optical and microphysical properties were characterized by exploiting both a multi-wavelength elastic-Raman lidar and a sun-sky-lunar photometer.

## 2. Materials and Methods

The Naples observation station for the aerosol remote sensing is part of the ACTRIS research infrastructure (Aerosol, Clouds and Trace Gases Research Infrastructure) [24].

As part of ACTRIS community, the instruments and algorithms have been quality assured through intercomparison experiments and several standard procedures; tools developed previously in the framework of the European Aerosol Research Lidar Network (EARLINET) are also available [25,26]. Tests for the quality assurance are regularly performed and submitted to the Center of Aerosol Remote Sensing (CARS) of ACTRIS in order to monitor the lidar measurements quality and to make the data ACTRIS compliant.

The station is located in Southern Italy (40.838° N, 14.183° E, 118 m a.s.l.) and its position is a crossroad of aerosols coming from different sources: sea spray aerosol from the Mediterranean Basin, urban and continental aerosol from the Central Europe, and Saharan dust from Northern Africa. Long range transported particles can also be observed, like aged biomass burning aerosol coming from Canada and North America regions during intense forest fire events. Measurements are routinely carried out with both passive and active ground based remote sensing instruments. Here, we will illustrate and discuss data registered by the lidar and sun-sky-lunar photometer of the observational station described hereafter.

### 2.1. MALIA multi-wavelength lidar

A multiwavelength Raman/elastic lidar system, MALIA, is used for the aerosol optical and microphysical characterization. The system uses as transmitter a Nd:YAG laser source providing beams at fundamental (1064 nm), second (532 nm) and third harmonics (355 nm) at a repetition rate of 20 Hz. The receiver is a Newtonian telescope with a focal length of 120 cm and a diameter of 30 cm. The lidar can retrieve Raman signals from N<sub>2</sub>, at wavelengths of 386 nm and 607 nm, and from H<sub>2</sub>O, at 407 nm. Data are acquired with 1-minute temporal resolution and 15 meters spatial resolution. MALIA can retrieve the aerosol backscatter  $\beta(z)$  profile at three different wavelengths (355 nm, 532 nm and 1064 nm) and the aerosol extinction profile  $\alpha(z)$  at two different wavelengths (355 nm and 532 nm), fulfilling the minimum requirements ( $3\beta + 2\alpha$ ) for the application of data inversion algorithms retrieving aerosol microphysical properties like refractive index and volume particle size distribution; in the present study, an inversion algorithm based on a Bayesian model run with Monte Carlo simulations was used [27,28]. The Klett–Fernald method [29,30] was exploited in order to obtain  $\beta(z)$  from elastic diurnal measurements, whereas the Raman method [31] was used for nocturnal measurements. The retrieval algorithms for aerosol optical properties comply with the EARLINET quality assurance program detailed in Ref. [32,33]. With the Raman method,  $\alpha(z)$  and  $\beta(z)$  are retrieved independently and the lidar ratio  $LR = \alpha(z)/\beta(z)$  can be estimated without any assumption.  $\beta(z)$  and  $\alpha(z)$  profiles are retrieved with a final spatial vertical resolution of 60m and 180m, respectively, and a temporal resolution of 30min. Errors in the retrieved parameters are evaluated using a Monte Carlo method that reproduce uncertainties in the  $\beta(z)$  and  $\alpha(z)$  final values in the range 5%-30% and 10-50%, respectively, at nighttime. MALIA can also perform depolarization measurements at 532 nm wavelength, obtaining the aerosol depolarization ratio  $\delta(z)$  from the lidar echo signals registered at the same and crossed polarizations with respect to the transmitted linearly polarized laser beam. Calibrated  $\delta(z)$  profiles are obtained using the inversion procedure described in Ref. [34] and Ref. [35]. LR and  $\delta$  can be used for aerosol typing, since both parameters depend on specific aerosol properties as size, shape, and refractive index. Finally, the backscattering Ångström exponent BAE (or color ratio) and extinction Ångstrom exponent EAE can also be retrieved using the relationships:

$$BAE = -\frac{\log\left(\frac{\beta(\lambda_1)}{\beta(\lambda_2)}\right)}{\log\left(\frac{\lambda_1}{\lambda_2}\right)}; EAE = -\frac{\log\left(\frac{\alpha(\lambda_1)}{\alpha(\lambda_2)}\right)}{\log\left(\frac{\lambda_1}{\lambda_2}\right)}$$

where  $\lambda_1 = 355$  nm and  $\lambda_2 = 532$  nm. Both these are intensive parameters that can provide useful information for aerosol properties classification. In particular, they are closely related to the aerosol size: higher values of the Ångström exponents are associated to a prevalence of particles with a smaller size [36]. Moreover, the combination of LR, depolarization ratio and Angstrom exponents can allow gaining more data for a reliable typing of the aerosol [37].

### 2.2. AERONET sun-photometer

Columnar aerosol measurements were carried out, simultaneously with lidar measurements, using a CIMEL CE318T [38], AERONET (Aerosol Robotic Network) [39,40] sun-sky-lunar photometer. The photometer collects daily radiance data at eight different wavelengths (340, 380, 440, 500, 675, 870, 1020 and 1640 nm) that through the inversion with AERONET algorithms [41,42] allow retrieving many optical and microphysical aerosol properties, like aerosol optical depth (AOD), Angstrom exponent ( $\alpha_{AE}$ ), volume particle size distribution, single scattering albedo (SSA), asymmetry factor, absorption AOD and real and imaginary part of the refractive index. The temporal variation and wavelength dependence of these parameters can provide information on the columnar properties of aerosol and on its evolution during the day. AOD is linked to the aerosol load in the atmospheric column, being related to the aerosol extinction. AOD values larger than 1 are representative of polluted atmospheric conditions, whereas AOD values less than 1 stand for clean atmosphere. The  $\alpha_{AE}$  parameter depends on the aerosol size and results larger than 1 when fine particles (e.g. black carbon or sulphate particles) are dominant; conversely, smaller  $\alpha_{AE}$  values are

indicative of aerosol with larger dimensions, corresponding mainly to coarse components (e.g. mineral dust or sea salt aerosol) [43]. In this study,  $\alpha_{AE}$  for the 440/870 nm wavelengths combination is used to gather information on the aerosol size [36]. The SSA is the ratio of the scattering process to the total (scattering and absorption) extinction and it is a key parameter in aerosol radiative forcing study; higher SSA values close to 1 are linked to more scattering aerosols (e.g., sulphate and nitrate), whereas values lower than 0.5 are indicative of more absorbing particles (e.g., black carbon, mineral dust and brown carbon) [44,45]. Particle size information is also given by the aerosol size distribution and the wavelength dependence of the asymmetry factor. The latter one is an important factor for assessing the aerosol radiative forcing. The absorption AOD considers only the absorption part of the total AOD. Together with the imaginary part of the refractive index and the SSA, it is important to study the absorption properties of the particles over the atmospheric column.

AERONET derived AOD has an estimated error of about 0.02 at 440 nm, as reported by Ref. [46], meanwhile  $\alpha_{AE}$  has an error of about 0.25 at the wavelengths of 440 and 870 nm for AOD larger than 0.1 [47]. Accurate error description for the inversion products are reported in Ref. [48]. Diurnal AOD and Ångström exponent level 2.0 quality controlled AERONET data are analyzed in this work, whereas only level 1.5 cloud-screened are available for lunar data and inversion products. Data are available in open access on <https://aeronet.gsfc.nasa.gov> (last visited on 16/12/2023).

### 2.3. Fire aerosol identification

The HYSPLIT (HYbrid Single-Particle Lagrangian Integrated Trajectory) model, developed by the U.S. National Atmospheric and Oceanic Administration (NOAA) Air Resources Laboratory (ARL) [49], is a well-established tool for the identification of aerosol source location. It can estimate the aerosol's back-trajectory for the days before its arrival on the station of interest using a hybrid Eulerian and Lagrangian mathematical approach. The model was used to calculate back-trajectories up to 20 days back from the date of interest and in a wide range of heights, locating the aerosol origin and the possible presence of other aerosol sources. This analysis allows to identify the different aerosol components that arrive over the observational station in a mixed state.

HYSPLIT model was used in synergy with the NASA Fire Information for Resource Management System (FIRMS) [50], developed in 2007 by the University of Maryland, for the identification of aged biomass burning aerosol that arrives over the observational station. It provides near real time fires data, derived from MODIS AQUA/TERRA and VIIRS instruments that are on board of satellites, on a global scale. Data are available in open access on <https://firms.modaps.eosdis.nasa.gov/> website (last visited on 16/12/2023).

In this study, the FIRMS model was used to identify fire events during August of 2017 for the Canadian region. Data were crossed with HYSPLIT back-trajectories to show the prevalent biomass burning composition of the aerosol layers arriving on the Naples observation station on 4<sup>th</sup> September 2017.

## 3. Data Analysis

During August 2017 intense fires developed in the British Columbia region (Canada), leading to the injection of an unusually high concentration of biomass burning aerosol in the atmosphere. Large amounts of fire smoke were lifted to the tropopause, even reaching the lower stratosphere. The lifting of these particles to the high troposphere was very fast due to the high radiative power of the wildfire event, preventing mixing with other aerosol or atmospheric constituents and leading to the peculiar compositional and shape properties observed for this event [19]. In the following weeks, higher altitudes layers of this aerosol were transported by winds from the source site throughout Europe, where they were observed in many locations and with different methodologies.

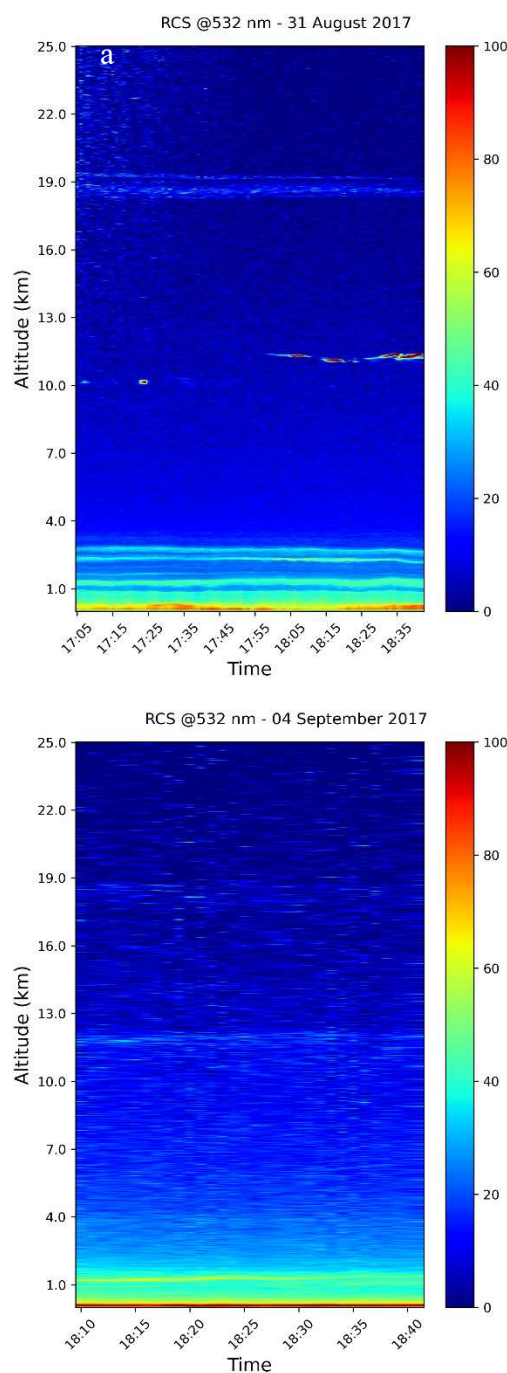


**Figure 1.** False color maps of the time series of the Range corrected Lidar Signal (RCS) measured at 532 nm. Panel (a) reports the observation corresponding to 31<sup>st</sup> August 2017, from 17:05 to 18:40, whereas panel (b) displays the situation registered on 4<sup>th</sup> September 2017, from 18:10 to 18:40. Times are shown in UTC.

A first signature of a stratospheric aerosol layer was observed over the Naples station, on 31<sup>st</sup> August 2017. This aerosol layer is clearly addressed in the map of the range corrected lidar signals (RCS) registered at 532 nm reported in Figure 1(a) and extends over an altitude range going from 18.2 to 19.4 km. In the same figure a clear signature of cirrus clouds is present at about 10-11 km of altitude. Unfortunately, it was not possible to characterize this aerosol layer at 355 nm and 1064 nm, due to the lower signal to noise ratio achieved for these two wavelengths at such a high altitude. Aerosol depolarization ratio at 532 nm was  $(16.7 \pm 5.5)\%$ ; such a value, which is rather unusual for inter-continental transported fire smoke particles, is in agreement with the observations described in other works reporting measurements carried out in the stratosphere over Europe [6–9].

The aerosol wildfire transport episode continued in the successive period, and a very interesting situation was registered on 4<sup>th</sup> September 2017, as displayed in Figure 1(b). The map of Figure 1(b) evidences the presence of various aerosol layers at different altitudes in the atmosphere over the station. Besides the persistence of a smoke aerosol layer at about 19 km, already addressed on 31<sup>st</sup> August 2017 in panel (a) of Figure 1, it is possible to recognize other three weak layers: the first extends from 11 to 13 km, the second is in the lower troposphere at an altitude between 2 and 4.5 km and the third below 2 km. A thorough characterization of these smoke aerosol layers can be carried out for the data reported in the map of Figure 1(b), since Raman measurements are also available in addition to the elastic ones. Hereafter, we will focus on this last observation with the aim of characterizing the features of these various aerosol layers.

Figure 2 illustrates the back-trajectories of the air masses that arrived over the measurement area on 4<sup>th</sup> September 2017 at the different altitude levels of interest for the three layers identified above. The HYSPLIT model clearly identifies Canada as the common origin of the observed layers; the symbols in the three panels of Figure 2 show FIRMS maps highlighting the locations of wildfires over the interested area, which was severely damaged by their intense activity during the August of 2017.

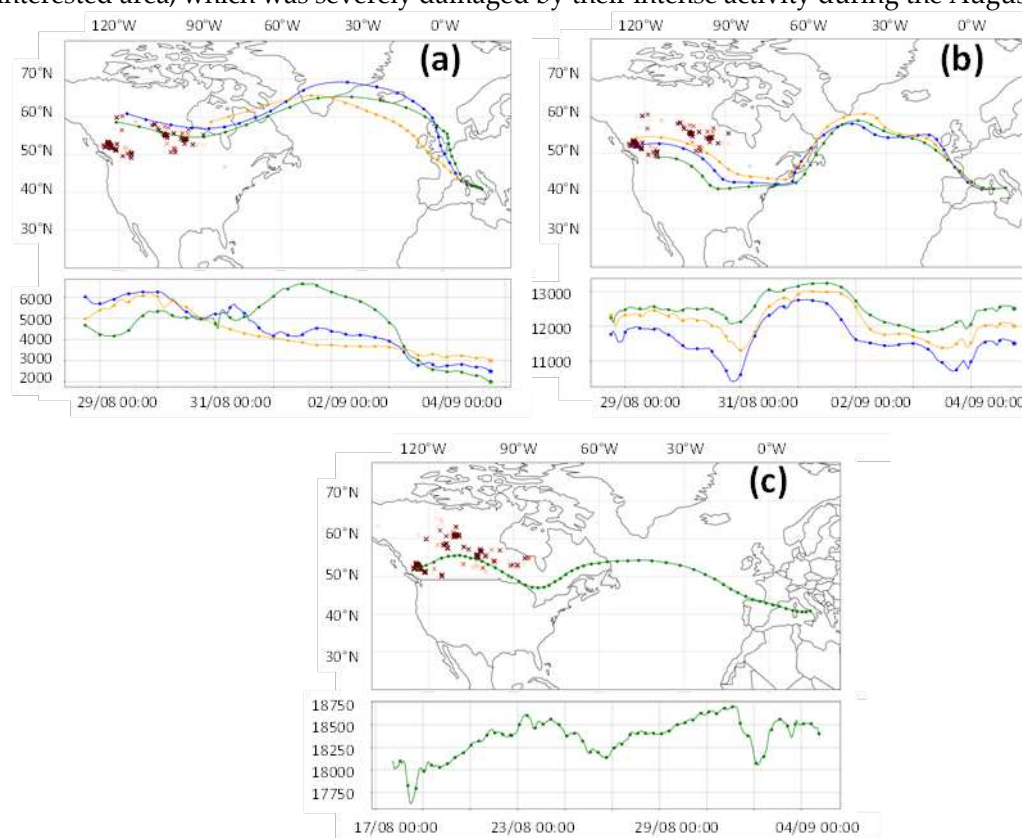


**Figure 2.** HYSPLIT back-trajectories ending over the measurement area on 4<sup>th</sup> September 2017 at 18:00 UTC. Red crosses represent hotspot fire location from FIRMS. For the troposphere layer (a) and the tropopause layer (b) FIRMS hot spot fire location are shown between 29<sup>th</sup> and 30<sup>th</sup> August 2017, whereas for the stratospheric layer (c) hotspot fire locations are shown between 17<sup>th</sup> and 18<sup>th</sup> August 2017.

The fire locations reported in the three maps of Figure 2 correspond to those observed in the days at which the back-trajectories, eventually ending over the observation station on 4<sup>th</sup> September 2017 at 18:00 UTC, passed over Canada. This analysis confirms that all the three layers observed by MALIA came from Canada and, therefore, are expected to present an important biomass burning component.

With the aim of characterizing the aerosol properties in each layer, we analyzed the lidar profiles measured at three wavelengths in terms of aerosol backscattering ( $\beta$ ), aerosol extinction ( $\alpha$ ) and

depolarization ratio ( $\delta$ ). 30 minutes time integrated lidar profiles (from 18:10 to 18:40 UTC) are reported in Figure 3.

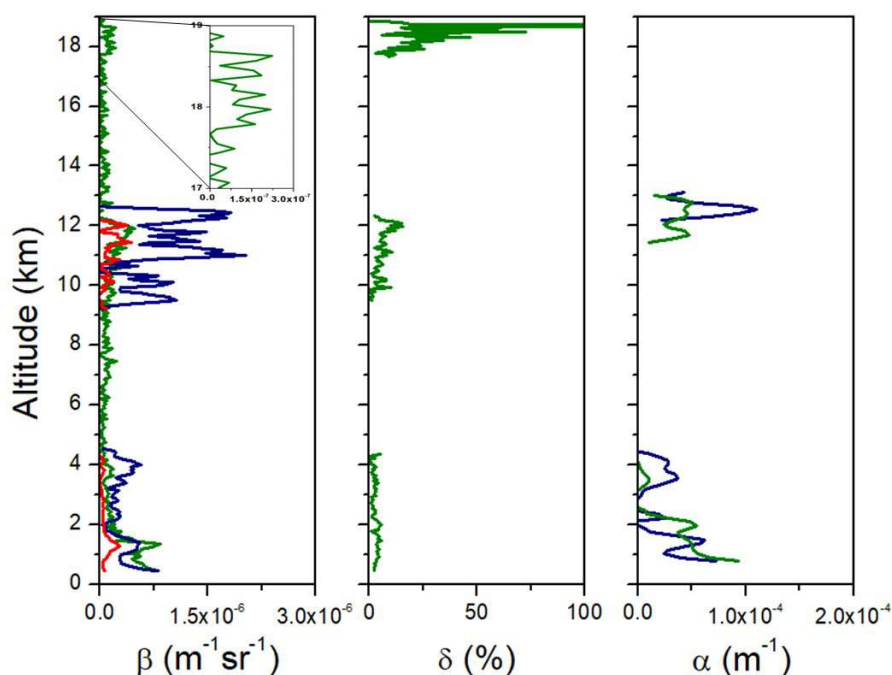


**Figure 3.** Lidar profiles of aerosol backscattering ( $\beta$ ), linear depolarization ratio ( $\delta$ ) and extinction ( $\alpha$ ) derived from the observations carried out from 18:10 to 18:40 UTC on 4<sup>th</sup> September 2017. The left panel displays the  $\beta$  profiles at the three wavelengths (red line – 1064 nm; green line – 532 nm; blue line – 355 nm); the inset shows a zoomed view of the 532 nm signal at high altitude evidencing the upper aerosol layer. The central panel reports the profile of  $\delta$  at 532 nm, whereas the right panel displays the profile of  $\alpha$  for the UV (blue line) and green (green line) wavelengths.

In the left panel of Figure 3, only the profile at 532 nm reaches an altitude up to 19 km due to the higher signal to noise ratio at these heights for such a wavelength, whereas the maximum level for the signals at 355 nm and 1064 nm is around 12-13 km. From the backscatter profiles in the left panel, the layers already identified in the false color map of the RCS signal in Figure 1(b) are clearly discernible. The backscatter and extinction profiles (left and right panels of Figure 3) allow estimating the average values of the Lidar Ratio (LR) for the layers located in the troposphere (range  $R_1$  and  $R_2$ ) and low stratosphere (range  $R_3$ ), respectively, for both 355 nm and 532 nm. For the tropospheric layers we estimate  $LR_{R1,355}=(32 \pm 10)$  and  $LR_{R1,532}=(82 \pm 17)$ ,  $LR_{R2,355}=(20 \pm 17)$  and  $LR_{R2,532}=(32 \pm 9)$ , whereas for the stratospheric one the values are  $LR_{R3,355}=(62 \pm 16)$  and  $LR_{R3,532}=(82 \pm 47)$ . The measured LR are in the range of values reported in the literature for biomass burning aerosols [19]; the lower LR values in the range  $R_2$  could be indicative of less absorbing particles in this layer [8]. The average aerosol depolarization ratios at 532 nm (central panel of Figure 3) for the layers located at  $R_1$ ,  $R_2$  and  $R_3$  are  $\delta_{R1}=(3.9 \pm 0.3)$  %,  $\delta_{R2}=(2.5 \pm 0.3)$  % and  $\delta_{R3}=(6.6 \pm 1.8)$  %, respectively; such values are suggestive of almost spherical smoke particles. In the range  $R_4$  (17.0-19.0 km) a higher value of  $\delta_{R4}=(29.8 \pm 7.6)$  % was measured, which is in agreement with those reported in previous works that investigated the summer 2017 inter-continental transport of smoke particles from Canada to Europe [6,8,9], addressing the higher value mainly to different transport ways and relative humidity conditions that lead to different aging processes.

Mean values of  $\beta(z)$  and  $\alpha(z)$  measured at 355 nm and 532 nm in the observed layers were used to retrieve the backscatter-related Ångström (BAE) and extinction-related Ångström (EAE) exponents, as well as the average values of the linear depolarization ratio ( $\delta$ ) and lidar ratio (LR). The estimated values of these lidar-derived aerosol parameters are summarized in Table 1. The values of BAE range from  $(1.1 \pm 0.7)$  to  $(4.4 \pm 4.9)$  and EAE varies from  $-(1.0 \pm 0.5)$  to  $(2.9 \pm 4.0)$ , in agreement with those reported in earlier works characterizing the properties of the biomass burning aerosol

layers observed in Europe. Ref. [51], analyzed the transport of biomass burning aerosol over Thessaloniki from regions with intense fire activity, reporting BAE values in the range 0.5-2.4. Moreover, in a recent study of Ref. [52] related to long term lidar observations of biomass burning aerosol over Warsaw, the EAE values range from -0.8 to 2.8, depending on the air masses origin, the lowest values corresponding to aged smoke particles. In the same study, the BAE values range from 1 to 2.7. In the present case, the retrieved values of BAE and EAE increase with altitude, although affected by a larger uncertainty for higher altitudes. This may indicate that the smoke particles in the ranges  $R_1$  and  $R_2$  have larger dimensions compared to those in the  $R_3$  range. Conversely, Ref. [19] in their study on western Canadian wildfire smoke observed in Leibniz measured higher values in the troposphere than in the stratosphere, which is suggestive of larger particles in the stratosphere probably related to different aging processes.

**Table 1.** Aerosol parameters measured in the smoke layers observed over Napoli area and derived by multi-wavelength lidar observations carried out on 4<sup>th</sup> September 2017.

Range (km)	$\delta$ (%)	LR <sub>355</sub>	LR <sub>532</sub>	BAE	EAE
R <sub>1</sub> (0.8-2.0)	3.9 ± 0.3	32 ± 10	82 ± 17	1.1 ± 0.7	-1.0 ± 0.5
R <sub>2</sub> (2.0-4.5)	2.5 ± 0.3	20 ± 17	32 ± 9	3.4 ± 2.1	-0.5 ± 3.0
R <sub>3</sub> (11.0-13.0)	6.6 ± 1.8	65 ± 35	82 ± 47	4.4 ± 4.9	2.9 ± 4.0
R <sub>4</sub> (17.0-19.0)	29.8 ± 7.6				

Mean values of  $\beta(z)$  and  $\alpha(z)$  measured at different wavelengths were also used to retrieve vertically resolved volume particle size distributions  $dV(r)/d\ln(r)$  (expressed in a.u.) [53]. The size distribution averaged over all the measured atmospheric column obtained from the lidar data is reported in Figure 4(a). The blue solid line refers to the mean value, whereas the two grey dotted curves define the error thresholds, corresponding to the minimum and maximum retrieved values. The lidar-derived size distribution, obtained from the profiles measured at about 18:00 UTC and discussed above, shows a bimodal shape with two peaks, whose mode radius values lie at about 0.20  $\mu\text{m}$  and 3.46  $\mu\text{m}$ . The lidar-derived size distribution results in fairly good agreement with the columnar particle size distribution provided by the AERONET sun-photometer data reported in Figure 4(b). In particular, for the AERONET size distribution measured at the time closest to the lidar observations, i.e. 14:42 UTC, the peak mode radius values sit at about 0.15  $\mu\text{m}$  and 3.86  $\mu\text{m}$ , respectively. The differences between the mode radii of the two distributions are likely due to the different measurement time intervals.

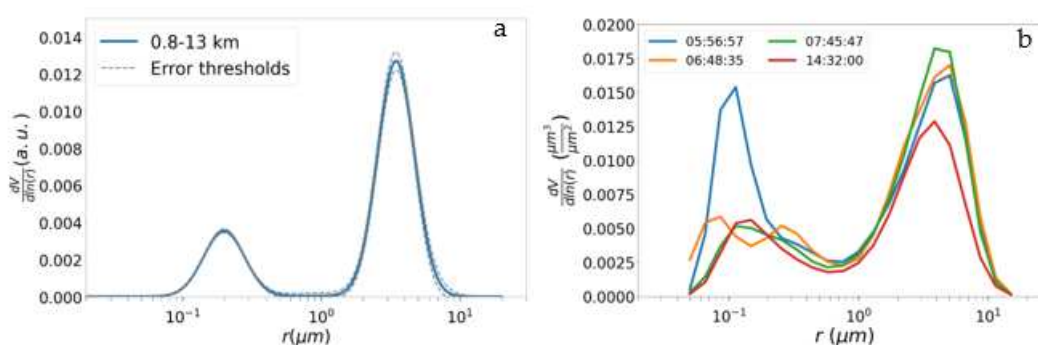


**Figure 4.** Columnar volume particle size distributions derived from lidar (a) and sun-photometer (b) data.  $dV(r)/d\ln(r)$  is the particles volume per unit of atmospheric surface and  $r$  is the particles radius.

The overall consistency of the columnar size distributions derived from lidar and sun-photometer data demonstrates the reliability of the lidar inversion algorithm, thus encouraging gaining further insights on the features of the three aerosol layers recognized in the map of Figure 1(b). In this respect, it is worth recalling that the size distribution derived from sun-photometer data is not vertically resolved; therefore, the possibility of gaining space resolved size distribution offered

by lidar is a unique and complementary source of information to characterize complex aerosol multi-layered conditions, as that occurred on 4<sup>th</sup> September 2017.

The lidar derived size distributions for the ranges  $R_1$ ,  $R_2$  and  $R_3$  are reported in Figure 5. All the three size distributions are bimodal, similarly to the columnar one discussed above (Figure 4). However, some interesting differences can be distinguished. For the higher layers at ranges  $R_2$  and  $R_3$ , a larger concentration of fine particles is observed, whose peak mode radius is about 0.2  $\mu\text{m}$  in both cases; the second, less populated fraction of particles is characterized by a peak mode radius of 5.2  $\mu\text{m}$  and 3.5  $\mu\text{m}$ , respectively, for the ranges  $R_2$  and  $R_3$ . A different situation is, instead, observed for the layer located at the range  $R_1$ , i.e. below 2 km of altitudes. For such a layer, the size distribution evidences a predominance of particles in the coarse mode fraction, with a peak radius of about 5.5  $\mu\text{m}$ . The comparison between the three size distributions in Figure 5 show that the relative fraction of the fine mode particles progressively increases with the altitude. The larger fraction of coarse particles observed in the lower troposphere can be rationalized as mainly due to deposition phenomena towards the ground.

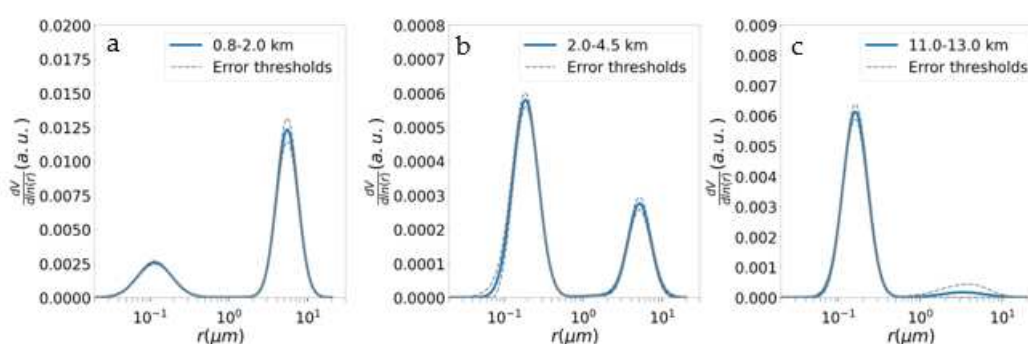


**Figure 5.** Volume particle size distributions as derived from lidar data for the three aerosol layers located at different ranges: (a)  $R_1$  (0.8-2.0 km), (b)  $R_2$  (2.0-4.5 km) and (c)  $R_3$  (11-13 km).

It is worth to notice that the predominance of the fine mode particles in the atmosphere revealed by the lidar data from 18:10 to 18:40 UTC agrees with the columnar aerosol properties derived by the sun-photometer. In fact, as shown in Figure 6, AERONET data evidence a progressive increase of the fine mode aerosol fraction in the atmospheric column since 14:00 UTC and an even larger dominance of the small particles (Fine Mode Fraction > 0.8) after 16:00 UTC.

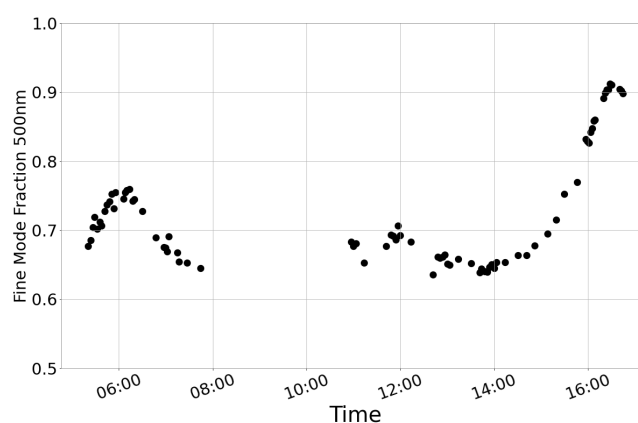


**Figure 6.** Fine mode Fraction at 500nm derived from AERONET data on 4<sup>th</sup> September 2017.

Further information on the aerosol features can be gained by resorting to the columnar parameters provided by the sun-photometer. The columnar  $\text{AOD}_{440}$  and  $\alpha_{440/870}$  measured by diurnal and nocturnal sun-photometer observations shows  $\text{AOD}_{440}$  and  $\alpha_{440/870}$  values larger than 0.1 and 1.3, respectively, namely in the afternoon (not shown). This observation, in turn, suggest a higher content of fine particles in the atmospheric column, in agreement with the analyses reported above. In

addition, as asserted by Ref. [54], the observed value of  $\alpha_{440/870}$  can be considered as representative of pure brown carbon or black carbon cores coated in non-absorbing matter.

The dominance of fine particles in the atmospheric column is further supported by the spectral dependence of the asymmetry factor reported in Figure 7a, which shows a decreasing trend with the wavelength in the afternoon that can be ascribed to a more efficient scattering at lower wavelengths typical of the fine aerosol. The observed values of the asymmetry factor below 0.7 at 440nm agree with those reported in the literature for biomass burning aerosol; for example, Ref. [8] registered a mean value of 0.7 at 440nm for aged smoke plumes observed in the Iberian Peninsula on 7<sup>th</sup> and 8<sup>th</sup> September 2017. Panels (b) and (c) of Figure 7 also show SSA and AOD absorption evidencing large values of the SSA (> 0.97) and low AOD absorption (< 0.0025) at 440 nm. These values are coherent with the results obtained in previous studies related to biomass burning aerosol, that reported SSA values in the range 0.91-0.99. For example, Ref. [55] estimated an average SSA at 440 nm ranging from 0.95 to 0.97 for smoke aerosol, with slightly larger values for more aged plumes. Moreover, studies on the biomass burning aerosol observed in Europe and originated from North America [8,56,57] attributed these values mainly to the transformation of the biomass burning aerosol and its mixing with non-absorbing aerosol species during their transport. Ref. [8] asserted that the low absorption (SSA>0.98) of the smoke particles observed over the Iberian Peninsula on 7<sup>th</sup> and 8<sup>th</sup> September 2017 might result from a smoldering combustion at the source, that gives rise to aerosol whose absorption properties are lower than those generated during a flaming phase.

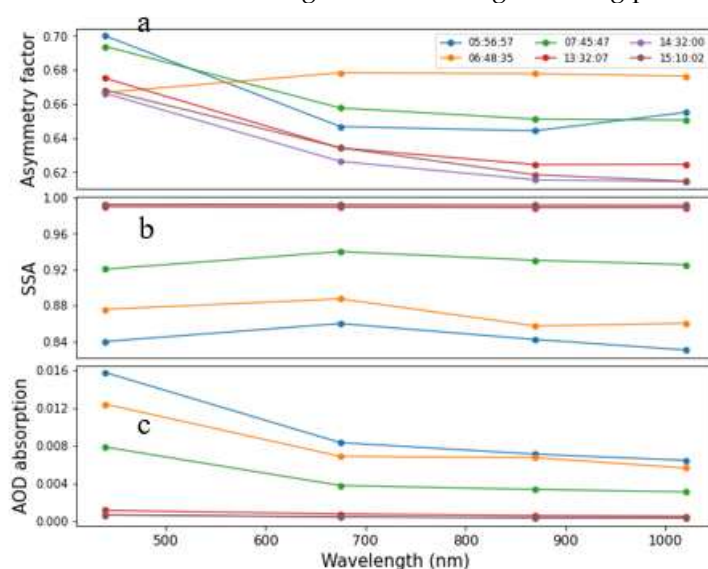


**Figure 7.** Wavelength dependence of Asymmetry factor (a), SSA (b) and AOD absorption (c) at different times derived from AERONET data on 4<sup>th</sup> September 2017. .

The high SSA values discussed above are associated to small values of the imaginary part of the refractive index, as shown in Figure 8, which since 13:32 UTC lowers to less than 0.001, suggesting a low black carbon fraction in the smoke particles probably due a predominance of smoldering combustion [58]. The spectral dependence of the imaginary part of the refractive index show a somewhat decreasing trend with the wavelength, possibly due to the absorption by organic carbon [59]. The real part of the refractive index in the afternoon in Figure 8 levels at a value of about 1.60 independently of the wavelength, whereas in the morning hours varies between 1.4 and 1.6. These values are consistent with those reported in the literature; for example, Ref. [60] observed values in the range 1.54-1.69 at 475 nm, with an average of  $(1.635 \pm 0.056)$  for the low black carbon fires, Ref. [61] measured values in the range 1.47-1.64 for biomass burning organic aerosol, showing that its variations could depend on the combustion efficiency. Moreover, values of the real part of the refractive index varying from 1.47 to 1.58 were also reported by Ref. [48] for biomass burning aerosol.

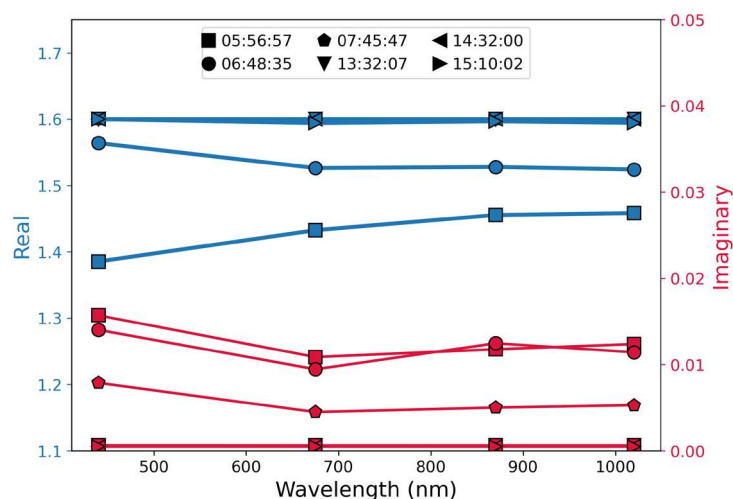


**Figure 8.** Wavelength dependence of real (blue lines, left axis) and imaginary (red lines, right axis) refractive index at different times (identified by different markers).

Finally, we would like to anticipate some results on the refractive index estimated by using an improved version of our lidar data inversion method [27] that will be the subject of a future publication [62]. These data are useful to further characterize the different aerosol layers recognized by the lidar measurement, since they provide slightly different values of the refractive index for the three aerosol layers located at the  $R_1$ ,  $R_2$  and  $R_3$  ranges. At a wavelength of 355 nm, the retrieved values of the refractive index are  $(1.4 \pm 0.03i)$  for  $R_1$ ,  $(1.5 \pm 0.008i)$  for  $R_2$ , and  $(1.4 \pm 0.01i)$  for  $R_3$ . The higher real refractive index in the layer at  $R_2$  could be due to the ageing processes occurred during the air masses transport; the lower imaginary part of the refractive index suggests a lower black carbon fraction in  $R_2$ , in agreement with lower LR values measured by lidar that suggested particles with a lower absorption at those altitudes [57]. In addition, the columnar value of the refractive index obtained by using our inversion method resulted to be  $(1.5 \pm 0.03i)$ , addressing a good consistency with the columnar data provided by the sun-photometer and also agreeing with the columnar values reported by other authors [63]. These observations eventually highlight that long-range transported aged smoke particles are less absorptive.

#### 4. Conclusions

Biomass burning aerosols arriving over Naples, Italy, from North America in 2017 were characterized in terms of their optical and microphysical properties with both a multi-wavelength elastic-Raman lidar of the ACTRIS research infrastructure and an AERONET sun-sky-lunar photometer.

Lidar profiles highlighted the presence of four aerosol layers. Two layers were located in the lower troposphere, namely below 2 km ( $R_1$ ) and in the range 2-4.5 km ( $R_2$ ), and the other two weak layers extended from 11 to 13 km ( $R_3$ ) and from 17 to 19 km ( $R_4$ ), respectively. Mean LR values at 355nm and 532nm in the first three layers were obtained and resulted to be equal to  $(32 \pm 10)$  and  $(82 \pm 17)$  for the  $R_1$  tropospheric layer,  $(20 \pm 17)$  and  $(32 \pm 9)$  for the  $R_2$  tropospheric layer and  $(62 \pm 16)$  and  $(82 \pm 47)$  for the lower stratospheric layer  $R_3$ , respectively. The aerosol depolarization ratio showed an increasing dependence on the altitude with averaged values of  $(3.9 \pm 0.3)\%$ ,  $(2.5 \pm 0.3)\%$ ,  $(5.5 \pm 0.5)\%$  and  $(29.8 \pm 7.6)\%$  for the different layers located at progressively larger heights, which is indicative of almost spherical smoke particles at the lower altitudes and aspheric particles at the highest range probably because of aging processes.

Volume particle size distributions were derived from the lidar data for the first three aerosol layers and highlighted that the particles observed in the troposphere have a slightly larger dimension than those present at higher altitude, mainly due to deposition phenomena towards the ground. Moreover, the layers located at ranges  $R_2$  and  $R_3$  related to smoke particles evidence a larger content of fine mode aerosol with peak mode radius values at  $0.2 \mu\text{m}$  and  $0.1 \mu\text{m}$ , respectively. Also,

AERONET columnar properties revealed a dominance of fine particles in the atmosphere with low absorption properties (absorption AOD < 0.0025 and SSA > 0.97) and addressed aerosol properties in good agreement with those evidenced by the lidar observations.

Finally, the refractive index for the three lower aerosol layers recognized by the lidar measurements was estimated by resorting to an inversion method capable of retrieving the microphysical particles properties. Our results, although preliminary, show a higher real part and a lower imaginary part of the refractive index in the R<sub>2</sub> later, suggesting a lower black carbon fraction and, in agreement with lower LR values measured by Lidar, less absorbing particles in this altitude range. Moreover, the space-resolved results on the refractive index are consistent with AERONET sun-photometer retrieved values, thus evidencing the reliability and capability of lidar characterization of atmospheric aerosol in a very interesting condition of multiple aerosol layers originating from Canadian fires overpassing the observation station.

**Acknowledgments:** The research leading to these results has received funding from the European Union's Horizon 2020 Framework Program for Research and Innovation (grant agreement no. 654109 – ACTRIS-2 Aerosols, Clouds, and Trace Gases Research InfraStructure) and from IR0000032 – ITINERIS, Italian Integrated Environmental Research Infrastructures System (D.D. n. 130/2022 - CUP B53C22002150006) Funded by EU - Next Generation EU PNRR- Mission 4 “Education and Research” - Component 2: “From research to business” - Investment 3.1: “Fund for the realisation of an integrated system of research and innovation infrastructures”. The authors gratefully acknowledge the NOAA Air Resource Laboratory (ARL) for provision the HYSPLIT transport and dispersion model and /or READY website used in this publication. Data and/or from the BSC-DREAM8b (Dust Regional Atmospheric Model) model were operated by the Barcelona Supercomputing Center (<http://www.bsc.es/ess/bsc-dust-daily-forecast/>). The authors thank ALA Advanced Lidar Applications s.r.l. for providing the PAPRICA software for the lidar microphysical properties retrieval.

**Conflicts of Interest:** The authors declare no conflict of interest. The funders had no role in the design of the study; in the collection, analyses, or interpretation of data; in the writing of the manuscript; or in the decision to publish the results.

## References

1. Linares, C.; Carmona, R.; Salvador, P.; Díaz, J. Impact on Mortality of Biomass Combustion from Wildfires in Spain: A Regional Analysis. *Science of The Total Environment* **2018**, *622–623*, 547–555, doi:10.1016/j.scitotenv.2017.11.321.
2. Alonso-Blanco, E.; Castro, A.; Calvo, A.I.; Pont, V.; Mallet, M.; Fraile, R. Wildfire Smoke Plumes Transport under a Subsidence Inversion: Climate and Health Implications in a Distant Urban Area. *Science of The Total Environment* **2018**, *619–620*, 988–1002, doi:10.1016/j.scitotenv.2017.11.142.
3. Reid, J.S.; Koppmann, R.; Eck, T.F.; Eleuterio, D.P. A Review of Biomass Burning Emissions Part II: Intensive Physical Properties of Biomass Burning Particles. *Atmospheric Chemistry and Physics* **2005**, *5*, 799–825, doi:10.5194/acp-5-799-2005.
4. Fiebig, M.; Petzold, A.; Wandinger, U.; Wendisch, M.; Kiemle, C.; Stifter, A.; Ebert, M.; Rother, T.; Leiterer, U. Optical Closure for an Aerosol Column: Method, Accuracy, and Inferable Properties Applied to a Biomass-Burning Aerosol and Its Radiative Forcing. *Journal of Geophysical Research: Atmospheres* **2002**, *107*, LAC 12-1-LAC 12-15, doi:10.1029/2000JD000192.
5. Hodshire, A.L.; Akherati, A.; Alvarado, M.J.; Brown-Steiner, B.; Jathar, S.H.; Jimenez, J.L.; Kreidenweis, S.M.; Lonsdale, C.R.; Onasch, T.B.; Ortega, A.M.; et al. Aging Effects on Biomass Burning Aerosol Mass and Composition: A Critical Review of Field and Laboratory Studies. *Environ. Sci. Technol.* **2019**, *53*, 10007–10022, doi:10.1021/acs.est.9b02588.
6. Ansmann, A.; Baars, H.; Chudnovsky, A.; Mattis, I.; Veselovskii, I.; Haarig, M.; Seifert, P.; Engelmann, R.; Wandinger, U. Extreme Levels of Canadian Wildfire Smoke in the Stratosphere over Central Europe on 21–22 August 2017. *Atmospheric Chemistry and Physics* **2018**, *18*, 11831–11845, doi:10.5194/acp-18-11831-2018.
7. Khaykin, S.M.; Godin-Beekmann, S.; Hauchecorne, A.; Pelon, J.; Ravetta, F.; Keckhut, P. Stratospheric Smoke With Unprecedentedly High Backscatter Observed by Lidars Above Southern France. *Geophysical Research Letters* **2018**, *45*, 1639–1646, doi:10.1002/2017GL076763.
8. Sicard, M.; Granados-Muñoz, M.J.; Alados-Arboledas, L.; Barragán, R.; Bedoya-Velásquez, A.E.; Benavent-Oltra, J.A.; Bortoli, D.; Comerón, A.; Córdoba-Jabonero, C.; Costa, M.J.; et al. Ground/Space, Passive/Active Remote Sensing Observations Coupled with Particle Dispersion Modelling to Understand the Inter-Continental Transport of Wildfire Smoke Plumes. *Remote Sensing of Environment* **2019**, *232*, 111294, doi:10.1016/j.rse.2019.111294.

9. Hu, Q.; Goloub, P.; Veselovskii, I.; Bravo-Aranda, J.-A.; Popovici, I.E.; Podvin, T.; Haeffelin, M.; Lopatin, A.; Dubovik, O.; Pietras, C.; et al. Long-Range-Transported Canadian Smoke Plumes in the Lower Stratosphere over Northern France. *Atmospheric Chemistry and Physics* **2019**, *19*, 1173–1193, doi:10.5194/acp-19-1173-2019.
10. Ohneiser, K.; Ansmann, A.; Witthuhn, J.; Deneke, H.; Chudnovsky, A.; Walter, G.; Senf, F. Self-Lofting of Wildfire Smoke in the Troposphere and Stratosphere: Simulations and Space Lidar Observations. *Atmospheric Chemistry and Physics* **2023**, *23*, 2901–2925, doi:10.5194/acp-23-2901-2023.
11. Rosenfeld, D.; Fromm, M.; Trentmann, J.; Luderer, G.; Andreae, M.O.; Servranckx, R. The Chisholm Firestorm: Observed Microstructure, Precipitation and Lightning Activity of a Pyro-Cumulonimbus. *Atmospheric Chemistry and Physics* **2007**, *7*, 645–659, doi:10.5194/acp-7-645-2007.
12. Ansmann, A.; Ohneiser, K.; Chudnovsky, A.; Knopf, D.A.; Eloranta, E.W.; Villanueva, D.; Seifert, P.; Radenz, M.; Barja, B.; Zamorano, F.; et al. Ozone Depletion in the Arctic and Antarctic Stratosphere Induced by Wildfire Smoke. *Atmospheric Chemistry and Physics* **2022**, *22*, 11701–11726, doi:10.5194/acp-22-11701-2022.
13. Alados-Arboledas, L.; Müller, D.; Guerrero-Rascado, J.L.; Navas-Guzmán, F.; Pérez-Ramírez, D.; Olmo, F.J. Optical and Microphysical Properties of Fresh Biomass Burning Aerosol Retrieved by Raman Lidar, and Star-and Sun-Photometry. *Geophysical Research Letters* **2011**, *38*, doi:10.1029/2010GL045999.
14. De Rosa, B.; Amato, F.; Amodeo, A.; D'Amico, G.; Dema, C.; Falconieri, A.; Giunta, A.; Gumà-Claramunt, P.; Kampouri, A.; Solomos, S.; et al. Characterization of Extremely Fresh Biomass Burning Aerosol by Means of Lidar Observations. *Remote Sensing* **2022**, *14*, 4984, doi:10.3390/rs14194984.
15. Ansmann, A.; Ohneiser, K.; Mamouri, R.-E.; Knopf, D.A.; Veselovskii, I.; Baars, H.; Engelmann, R.; Foth, A.; Jimenez, C.; Seifert, P.; et al. Tropospheric and Stratospheric Wildfire Smoke Profiling with Lidar: Mass, Surface Area, CCN, and INP Retrieval. *Atmospheric Chemistry and Physics* **2021**, *21*, 9779–9807, doi:10.5194/acp-21-9779-2021.
16. Baars, H.; Radenz, M.; Floutsi, A.A.; Engelmann, R.; Althausen, D.; Heese, B.; Ansmann, A.; Flament, T.; Dabas, A.; Trajon, D.; et al. Californian Wildfire Smoke Over Europe: A First Example of the Aerosol Observing Capabilities of Aeolus Compared to Ground-Based Lidar. *Geophysical Research Letters* **2021**, *48*, e2020GL092194, doi:10.1029/2020GL092194.
17. Adam, M.; Pahlow, M.; Kovalev, V.A.; Ondov, J.M.; Parlange, M.B.; Nair, N. Aerosol Optical Characterization by Nephelometer and Lidar: The Baltimore Supersite Experiment during the Canadian Forest Fire Smoke Intrusion. *Journal of Geophysical Research: Atmospheres* **2004**, *109*, doi:10.1029/2003JD004047.
18. Kloss, C.; Berthet, G.; Sellitto, P.; Ploeger, F.; Bucci, S.; Khaykin, S.; Jégou, F.; Taha, G.; Thomason, L.W.; Barret, B.; et al. Transport of the 2017 Canadian Wildfire Plume to the Tropics via the Asian Monsoon Circulation. *Atmospheric Chemistry and Physics* **2019**, *19*, 13547–13567, doi:10.5194/acp-19-13547-2019.
19. Haarig, M.; Ansmann, A.; Baars, H.; Jimenez, C.; Veselovskii, I.; Engelmann, R.; Althausen, D. Depolarization and Lidar Ratios at 355, 532, and 1064 nm and Microphysical Properties of Aged Tropospheric and Stratospheric Canadian Wildfire Smoke. *Atmospheric Chemistry and Physics* **2018**, *18*, 11847–11861, doi:10.5194/acp-18-11847-2018.
20. Baars, H.; Ansmann, A.; Ohneiser, K.; Haarig, M.; Engelmann, R.; Althausen, D.; Hanssen, I.; Gausa, M.; Pietruczuk, A.; Szkop, A.; et al. The Unprecedented 2017–2018 Stratospheric Smoke Event: Decay Phase and Aerosol Properties Observed with the EARLINET. *Atmospheric Chemistry and Physics* **2019**, *19*, 15183–15198, doi:10.5194/acp-19-15183-2019.
21. Peterson, D.A.; Fromm, M.D.; McRae, R.H.D.; Campbell, J.R.; Hyer, E.J.; Taha, G.; Camacho, C.P.; Kablick, G.P.; Schmidt, C.C.; DeLand, M.T. Australia's Black Summer Pyrocumulonimbus Super Outbreak Reveals Potential for Increasingly Extreme Stratospheric Smoke Events. *npj Clim Atmos Sci* **2021**, *4*, 1–16, doi:10.1038/s41612-021-00192-9.
22. Ohneiser, K.; Ansmann, A.; Baars, H.; Seifert, P.; Barja, B.; Jimenez, C.; Radenz, M.; Teisseire, A.; Floutsi, A.; Haarig, M.; et al. Smoke of Extreme Australian Bushfires Observed in the Stratosphere over Punta Arenas, Chile, in January 2020: Optical Thickness, Lidar Ratios, and Depolarization Ratios at 355 and 532 nm. *Atmospheric Chemistry and Physics* **2020**, *20*, 8003–8015, doi:10.5194/acp-20-8003-2020.
23. Ohneiser, K.; Ansmann, A.; Kaifler, B.; Chudnovsky, A.; Barja, B.; Knopf, D.A.; Kaifler, N.; Baars, H.; Seifert, P.; Villanueva, D.; et al. Australian Wildfire Smoke in the Stratosphere: The Decay Phase in 2020/2021 and Impact on Ozone Depletion. *Atmospheric Chemistry and Physics* **2022**, *22*, 7417–7442, doi:10.5194/acp-22-7417-2022.
24. Wandinger, U.; Nicolae, D.; Pappalardo, G.; Mona, L.; Comerón, A. ACTRIS and Its Aerosol Remote Sensing Component. *EPJ Web Conf.* **2020**, *237*, 05003, doi:10.1051/epjconf/202023705003.
25. Freudenthaler, V.; Linné, H.; Chaikovski, A.; Rabus, D.; Groß, S. EARLINET Lidar Quality Assurance Tools. *Atmospheric Measurement Techniques Discussions* **2018**, 1–35, doi:10.5194/amt-2017-395.
26. Wandinger, U.; Freudenthaler, V.; Baars, H.; Amodeo, A.; Engelmann, R.; Mattis, I.; Groß, S.; Pappalardo, G.; Giunta, A.; D'Amico, G.; et al. EARLINET Instrument Intercomparison Campaigns: Overview on Strategy and Results. *Atmospheric Measurement Techniques* **2016**, *9*, 1001–1023, doi:10.5194/amt-9-1001-2016.

27. Sorrentino, A.; Sannino, A.; Spinelli, N.; Piana, M.; Boselli, A.; Tontodonato, V.; Castellano, P.; Wang, X. A Bayesian Parametric Approach to the Retrieval of the Atmospheric Number Size Distribution from Lidar Data. *Atmospheric Measurement Techniques* **2022**, *15*, 149–164, doi:10.5194/amt-15-149-2022.
28. Samoilova, S.V. Simultaneous Reconstruction of the Complex Refractive Index and the Particle Size Distribution Function from Lidar Measurements: Testing the Developed Algorithms. *Atmos Ocean Opt* **2019**, *32*, 628–642, doi:10.1134/S1024856019060137.
29. Klett, J.D. Stable Analytical Inversion Solution for Processing Lidar Returns. *Appl. Opt., AO* **1981**, *20*, 211–220, doi:10.1364/AO.20.000211.
30. Fernald, F.G. Analysis of Atmospheric Lidar Observations: Some Comments. *Appl. Opt., AO* **1984**, *23*, 652–653, doi:10.1364/AO.23.000652.
31. Ansmann, A.; Riebesell, M.; Wandinger, U.; Weitkamp, C.; Voss, E.; Lahmann, W.; Michaelis, W. Combined Raman Elastic-Backscatter LIDAR for Vertical Profiling of Moisture, Aerosol Extinction, Backscatter, and LIDAR Ratio. *Appl. Phys. B* **1992**, *55*, 18–28, doi:10.1007/BF00348608.
32. Böckmann, C.; Wandinger, U.; Ansmann, A.; Bösenberg, J.; Amiridis, V.; Boselli, A.; Delaval, A.; Tomasi, F.D.; Frioud, M.; Grigorov, I.V.; et al. Aerosol Lidar Intercomparison in the Framework of the EARLINET Project. 2. Aerosol Backscatter Algorithms. *Appl. Opt., AO* **2004**, *43*, 977–989, doi:10.1364/AO.43.000977.
33. Pappalardo, G.; Amodeo, A.; Pandolfi, M.; Wandinger, U.; Ansmann, A.; Bösenberg, J.; Matthias, V.; Amiridis, V.; De Tomasi, F.; Frioud, M.; et al. Aerosol Lidar Intercomparison in the Framework of the EARLINET Project. 3. Raman Lidar Algorithm for Aerosol Extinction, Backscatter, and Lidar Ratio. *Applied optics* **2004**, *43*, 5370–5385, doi:10.1364/AO.43.005370.
34. Biele, J.; Beyerle, G.; Baumgarten, G. Polarization Lidar: Corrections of Instrumental Effects. *Opt. Express, OE* **2000**, *7*, 427–435, doi:10.1364/OE.7.000427.
35. Freudenthaler, V.; Esselborn, M.; Wiegner, M.; Heese, B.; Tesche, M.; Ansmann, A.; Müller, D.; Althausen, D.; Wirth, M.; Fix, A.; et al. Depolarization Ratio Profiling at Several Wavelengths in Pure Saharan Dust during SAMUM 2006. *Tellus B* **2009**, *61*, 165–179, doi:10.1111/j.1600-0889.2008.00396.x.
36. Schuster, G.L.; Dubovik, O.; Holben, B.N. Angstrom Exponent and Bimodal Aerosol Size Distributions. *Journal of Geophysical Research: Atmospheres* **2006**, *111*, doi:10.1029/2005JD006328.
37. Song, Y.; Zhang, B.; Shi, G.; Li, S.; Di, H.; Yan, Q.; Hua, D. Correlation between the Lidar Ratio and the Ångström Exponent of Various Aerosol Types. *Particuology* **2018**, *40*, 62–69, doi:10.1016/j.partic.2017.12.002.
38. Barreto, Á.; Cuevas, E.; Granados-Muñoz, M.-J.; Alados-Arboledas, L.; Romero, P.M.; Gröbner, J.; Kouremeti, N.; Almansa, A.F.; Stone, T.; Toledano, C.; et al. The New Sun-Sky-Lunar Cimel CE318-T Multiband Photometer &ndash; a Comprehensive Performance Evaluation. *Atmospheric Measurement Techniques* **2016**, *9*, 631–654, doi:10.5194/amt-9-631-2016.
39. Holben, B.N.; Eck, T.F.; Slutsker, I.; Tanré, D.; Buis, J.P.; Setzer, A.; Vermote, E.; Reagan, J.A.; Kaufman, Y.J.; Nakajima, T.; et al. AERONET—A Federated Instrument Network and Data Archive for Aerosol Characterization. *Remote Sensing of Environment* **1998**, *66*, 1–16, doi:10.1016/S0034-4257(98)00031-5.
40. Rolph, G.; Stein, A.; Stunder, B. Real-Time Environmental Applications and Display sYstem: READY. *Environmental Modelling & Software* **2017**, *95*, 210–228, doi:10.1016/j.envsoft.2017.06.025.
41. Dubovik, O.; King, M. A Flexible Inversion Algorithm for Retrieval of Aerosol Optical Properties from Sun and Sky Radiance Measurements. *Journal of Geophysical Research* **2000**, *105696*, 673–20, doi:10.1029/2000JD900282.
42. Holben, B.N.; Tanré, D.; Smirnov, A.; Eck, T.F.; Slutsker, I.; Abuhassan, N.; Newcomb, W.W.; Schafer, J.S.; Chatenet, B.; Lavenu, F.; et al. An Emerging Ground-Based Aerosol Climatology: Aerosol Optical Depth from AERONET. *Journal of Geophysical Research: Atmospheres* **2001**, *106*, 12067–12097, doi:10.1029/2001JD900014.
43. Huang, K.; Fu, J.S.; Lin, N.-H.; Wang, S.-H.; Dong, X.; Wang, G. Superposition of Gobi Dust and Southeast Asian Biomass Burning: The Effect of Multisource Long-Range Transport on Aerosol Optical Properties and Regional Meteorology Modification. *Journal of Geophysical Research: Atmospheres* **2019**, *124*, 9464–9483, doi:10.1029/2018JD030241.
44. Bergstrom, R.W.; Pilewskie, P.; Russell, P.B.; Redemann, J.; Bond, T.C.; Quinn, P.K.; Sierau, B. Spectral Absorption Properties of Atmospheric Aerosols. *Atmospheric Chemistry and Physics* **2007**, *7*, 5937–5943, doi:10.5194/acp-7-5937-2007.
45. Wang, S.-H.; Lin, N.-H.; Chou, M.-D.; Woo, J.-H. Estimate of Radiative Forcing of Asian Biomass-Burning Aerosols during the Period of TRACE-P. *Journal of Geophysical Research: Atmospheres* **2007**, *112*, doi:10.1029/2006JD007564.
46. Eck, T.; Holben, B.N.; Reid, J.; Dubovik, O.; Smirnov, A.; Neill; Slutsker, I.; Kinne, S. Wavelength Dependence of the Optical Depth of Biomass Burning, Urban, and Desert Dust Aerosols. *J. Geophys. Res.* **1999**, *104349*, 333–31, doi:10.1029/1999JD900923.
47. Toledano, C.; Cachorro, V.E.; Berjon, A.; de Frutos, A.M.; Sorribas, M.; de la Morena, B.A.; Goloub, P. Aerosol optical depth and Ångström exponent climatology at El Arenosillo AERONET site (Huelva, Spain). *Quarterly Journal of the Royal Meteorological Society* **2007**, *133*, 795–807, doi:10.1002/qj.54.

48. Dubovik, O.; Smirnov, A.; Holben, B.N.; King, M.D.; Kaufman, Y.J.; Eck, T.F.; Slutsker, I. Accuracy Assessments of Aerosol Optical Properties Retrieved from Aerosol Robotic Network (AERONET) Sun and Sky Radiance Measurements. *Journal of Geophysical Research: Atmospheres* **2000**, *105*, 9791–9806, doi:10.1029/2000JD900040.
49. Stein, A.F.; Draxler, R.R.; Rolph, G.D.; Stunder, B.J.B.; Cohen, M.D.; Ngan, F. NOAA's HYSPLIT Atmospheric Transport and Dispersion Modeling System. *Bulletin of the American Meteorological Society* **2015**, *96*, 2059–2077, doi:10.1175/BAMS-D-14-00110.1.
50. Davies, D.K.; Ilavajhala, S.; Wong, M.M.; Justice, C.O. Fire Information for Resource Management System: Archiving and Distributing MODIS Active Fire Data. *IEEE Transactions on Geoscience and Remote Sensing* **2009**, *47*, 72–79, doi:10.1109/TGRS.2008.2002076.
51. Amiridis, V.; Balis, D.S.; Giannakaki, E.; Stohl, A.; Kazadzis, S.; Koukouli, M.E.; Zanis, P. Optical Characteristics of Biomass Burning Aerosols over Southeastern Europe Determined from UV-Raman Lidar Measurements. *Atmospheric Chemistry and Physics* **2009**, *9*, 2431–2440, doi:10.5194/acp-9-2431-2009.
52. Janicka, L.; Davulienė, L.; Bycenkiene, S.; Stachlewska, I.S. Long Term Observations of Biomass Burning Aerosol over Warsaw by Means of Multiwavelength Lidar. *Opt. Express, OE* **2023**, *31*, 33150–33174, doi:10.1364/OE.496794.
53. Sannino, A.; Amoroso, S.; Damiano, R.; Scollo, S.; Sellitto, P.; Boselli, A. Optical and Microphysical Characterization of Atmospheric Aerosol in the Central Mediterranean during Simultaneous Volcanic Ash and Desert Dust Transport Events. *Atmospheric Research* **2022**, *271*, doi:10.1016/j.atmosres.2022.106099.
54. Lack, D.A.; Cappa, C.D. Impact of Brown and Clear Carbon on Light Absorption Enhancement, Single Scatter Albedo and Absorption Wavelength Dependence of Black Carbon. *Atmospheric Chemistry and Physics* **2010**, *10*, 4207–4220, doi:10.5194/acp-10-4207-2010.
55. Nikonovas, T.; North, P.R.J.; Doerr, S.H. Smoke Aerosol Properties and Ageing Effects for Northern Temperate and Boreal Regions Derived from AERONET Source and Age Attribution. *Atmospheric Chemistry and Physics* **2015**, *15*, 7929–7943, doi:10.5194/acp-15-7929-2015.
56. Markowicz, K.M.; Chilinski, M.T.; Lisok, J.; Zawadzka, O.; Stachlewska, I.S.; Janicka, L.; Rozwadowska, A.; Makuch, P.; Pakszys, P.; Zielinski, T.; et al. Study of Aerosol Optical Properties during Long-Range Transport of Biomass Burning from Canada to Central Europe in July 2013. *Journal of Aerosol Science* **2016**, *101*, 156–173, doi:10.1016/j.jaerosci.2016.08.006.
57. Ortiz-Amezcu, P.; Guerrero-Rascado, J.L.; Granados-Muñoz, M.J.; Benavent-Oltra, J.A.; Böckmann, C.; Samaras, S.; Stachlewska, I.S.; Janicka, L.; Baars, H.; Bohlmann, S.; et al. Microphysical Characterization of Long-Range Transported Biomass Burning Particles from North America at Three EARLINET Stations. *Atmospheric Chemistry and Physics* **2017**, *17*, 5931–5946, doi:10.5194/acp-17-5931-2017.
58. Eck, T.F.; Holben, B.N.; Reid, J.S.; Sinyuk, A.; Hyer, E.J.; O'Neill, N.T.; Shaw, G.E.; Castle, J.R.V.; Chapin, F.S.; Dubovik, O.; et al. Optical Properties of Boreal Region Biomass Burning Aerosols in Central Alaska and Seasonal Variation of Aerosol Optical Depth at an Arctic Coastal Site. *Journal of Geophysical Research. Vol.114: D11201* **2009**.
59. Kirchstetter, T.W.; Novakov, T.; Hobbs, P.V. Evidence That the Spectral Dependence of Light Absorption by Aerosols Is Affected by Organic Carbon. *Journal of Geophysical Research: Atmospheres* **2004**, *109*, doi:10.1029/2004JD004999.
60. Womack, C.C.; Manfred, K.M.; Wagner, N.L.; Adler, G.; Franchin, A.; Lamb, K.D.; Middlebrook, A.M.; Schwarz, J.P.; Brock, C.A.; Brown, S.S.; et al. Complex Refractive Indices in the Ultraviolet and Visible Spectral Region for Highly Absorbing Non-Spherical Biomass Burning Aerosol. *Atmospheric Chemistry and Physics* **2021**, *21*, 7235–7252, doi:10.5194/acp-21-7235-2021.
61. Luo, B.; Kuang, Y.; Huang, S.; Song, Q.; Hu, W.; Li, W.; Peng, Y.; Chen, D.; Yue, D.; Yuan, B.; et al. Parameterizations of Size Distribution and Refractive Index of Biomass Burning Organic Aerosol with Black Carbon Content. *Atmospheric Chemistry and Physics* **2022**, *22*, 12401–12415, doi:10.5194/acp-22-12401-2022.
62. Sannino, A.; Damiano, R.; Sorrentino, A.; Spinelli, N.; Wang, X.; Boselli, A. Retrieving Atmospheric Number Size Distribution and Complex Refractive Index from Lidar Data. **2024**. *To be submitted*
63. López-Cayuela, M.-Á.; Herrera, M.E.; Córdoba-Jabonero, C.; Pérez-Ramírez, D.; Carvajal-Pérez, C.V.; Dubovik, O.; Guerrero-Rascado, J.L. Retrieval of Aged Biomass-Burning Aerosol Properties by Using GRASP Code in Synergy with Polarized Micro-Pulse Lidar and Sun/Sky Photometer. *Remote Sensing* **2022**, *14*, 3619, doi:10.3390/rs14153619.

**Disclaimer/Publisher's Note:** The statements, opinions and data contained in all publications are solely those of the individual author(s) and contributor(s) and not of MDPI and/or the editor(s). MDPI and/or the editor(s) disclaim responsibility for any injury to people or property resulting from any ideas, methods, instructions or products referred to in the content.